Controlling Extrudate Volume Fraction through Poroelastic Extrusion of Entangled Fibers

Zehao Pan
Princeton University
Janine Nunes
Princeton University
Camille Duprat
Princeton University
Ho Shum
University of Hong Kong https://orcid.org/0000-0002-6365-8825
Howard Stone (hastone@princeton.edu)
Princeton University https://orcid.org/0000-0002-9670-0639

Article

Keywords: poroelasticity, microfiber, suspension, entanglements

Posted Date: August 19th, 2022

DOI: https://doi.org/10.21203/rs.3.rs-1925965/v1

Many materials systems consist of mixtures of particles of various shapes, and readily deform and flow. For example, when a suspension of spherical or near-spherical particles passes through a constriction the volume fraction either remains the same or decreases. In contrast to these particle suspensions, here we observe that an entangled fiber suspension increases its volume fraction up to 14-fold after passing through a constriction. We attribute this response to the entanglements among the fibers that allows the network to move faster than the liquid. By changing the fiber geometry, we find that the entanglements originate from interlocking shapes or high flexibility. A quantitative poroelastic model is used to explain the increase in velocity and extrudate volume fractions. These results provide a new strategy to control soft materials, e.g., suspension concentration and porosity, during delivery, as occurs in healthcare, three-dimensional printing, or material repair.

Controlling Extrudate Volume Fraction through Poroelastic Extrusion of Entangled Fibers

Zehao Pan[1], Janine K. Nunes[1], Camille Duprat[2], Ho Cheung Shum[3] and Howard A. Stone[1*]

[1]Department of Mechanical and Aerospace Engineering, Princeton University, Princeton, NJ 08544.
[2]LadHyX - École Polytechnique, Palaiseau Cedex 91128, France.
[3]Department of Mechanical Engineering, University of Hong Kong, Pokfulam Road, Hong Kong, 999077 China.

*Corresponding author(s). E-mail(s): hastone@princeton.edu;

Keywords: poroelasticity, microfiber, suspension, entanglements

Injectable biomaterials are used widely as cavity-filling agents, such as in the treatments of aneurysms [1], spinal cord regeneration [2], and wound dressings [3, 4]. In these applications, it is desirable during the delivery that the material should have good flowability to facilitate movement in a thin catheter or needle. After delivery, the material should transition rapidly to poor flowability to prevent egress. Suspensions have emerged as an attractive candidate for this class of materials [5], whose rheological response is coupled to the

local volume fraction. However, it remains a challenge to create a suspension with low concentration during material delivery to facilitate flow and high concentration at the delivered site to ensure material localization and functionality.

When pushed through a constriction, a dense particulate suspension made of spherical or near-spherical particles can suffer from "demixing" [6], "liquid migration" [7, 8], "self-filtration" [9, 10] or "dilatancy" [11], where the liquid moves relative to the solid phase, producing a more dilute mixture at the exit of a constriction. So far, most research on the extrusion of suspensions has been focused on particulate systems.

However, suspensions made from fibers can be mechanically distinct from their spherical and near-spherical counterparts in their ability to respond elastically to tensile stresses. In the absence of permanent linkages, entanglements among different fibers can arise from static friction, irregular shapes, and interlocking structures [12–16]. When the density of these linkages reaches a threshold, the suspension starts to respond as a soft elastic material [17]. These entanglements offer the fiber network stability under moderate shear or extensional flow conditions [18], where the elasticity of such entangled fiber networks has been studied using simulations [17, 19, 20]. In addition, the rheological properties of fiber suspensions have been studied in the context of paper pulp [21–23]. Currently, there is a lack of experimental studies and insights on the permeability and elasticity of entangled fiber suspensions due to difficulty in measurements. As a result, their volume fraction variations are not fully understood and the dynamical responses in a flow field we report here have not been recognized previously.

When used as a biomaterial, fiber suspensions offer several unique properties. The fibers can be readily made from existing biocompatible materials for

toxicity-sensitive applications using established fiber spinning methods [24]. A loose packing of fibers can also create a gel with hierarchical porosity where the pore sizes range from the scale of molecular cross links in the fiber to the typical distance between fibers in a suspension [25, 26]. Hence, from a material design perspective, in order to control the mechanical and transport properties, it is important to understand how the volume fraction of such a soft elastic material changes upon extrusion.

In this paper, we experimentally characterized the flow field and volume fraction variations when suspensions of designed flexible, micro-textured, and entangled microfibers pass through a constriction. As the microfibers enter the constriction, instead of the commonly observed "self-filtration", the faster moving fibers in the constriction cause elastic stretching among the entangled fibers upstream of the constriction. As a result, the suspension downstream of the constriction has an *increased volume fraction*. We model the process based on a poroelastic framework that takes into account the coupling between the elastic deformation and the flow within the network of entangled fibers. Our work may also inspire modelling of similar processes such as the injection of granular materials with dynamic bonds [27] and biologically active networks [28].

Results

Fiber suspensions passing a constriction

The poly(ethylene glycol) diacrylate (PEGDA) fibers were made using a jet-assisted wet spinning (JAWS) method described in *Materials and Methods*. A custom-made transparent channel with rectangular cross section (8 mm in depth by 10 mm in width) was used to visualize the microfiber suspensions as they pass through a constriction.

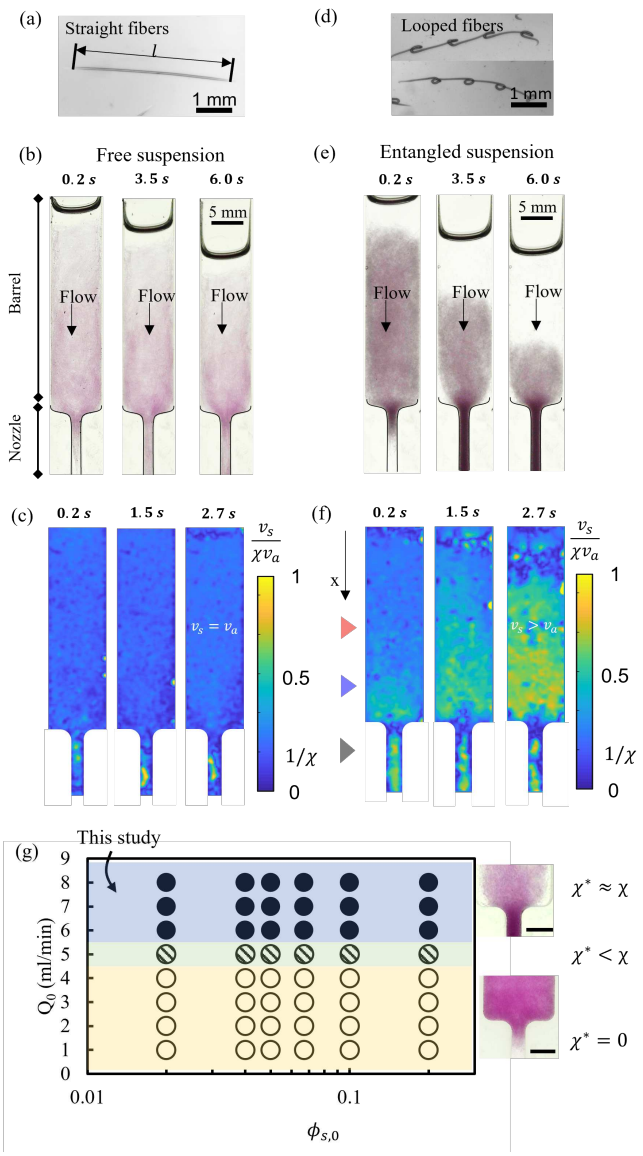

Fig. 1 Concentration and velocity variations when suspensions of straight and looped fibers pass a constriction. (a) and (d): Shapes of the straight and looped fibers, respectively. (b) and (e): Snapshots of suspensions of (a) straight and (d) looped fibers flowing through a constriction when a constant flow rate of 8 ml/min is applied. The initial fiber volume fractions $\phi_{s,0}$ are 0.2 for both cases. (c) and (f): Velocity (x component) distributions of the straight and looped fibers from PIV measurements of the experiments in, respectively, (b) and (e) at three different times. The fiber velocity v_s is normalized by the average velocity in the nozzle χv_a. The colored triangles to the left of (f) are positions measured in Fig. 3(e). (g) Regime map for the extrusion of a looped fiber suspension as a function of Q_0 and $\phi_{s,0}$ using a Norm-ject 5 ml syringe. No fibers can flow out the constriction when $Q_0 < 5$ ml/min (clogging regime, $\chi^* = 0$). For a flow rate $Q_0 \approx 5$ ml/min, the fibers start flowing intermittently with $\chi^* < \chi$.

We first tested the extrusion of stiff straight fibers with diameter $d = 60\ \mu$m, length $l = 4.3$ mm, and aspect ratio $l/d = 72$ (Fig. 1(a)). Before the experiment, a suspension of straight fibers was introduced in an open barrel with an initial volume fraction of $\phi_{s,0} = 0.2$. At $t = 0$ s, a constant withdrawal flow rate $Q_0 = 8$ ml/min was applied through a syringe at the end of the nozzle, which drew the suspension from the barrel into the nozzle. Snapshots of the experiment are shown in Fig. 1(b). The fibers in the barrel moved with the surrounding fluid without being dragged into the nozzle by the other fibers and the volume fraction in the nozzle was largely unchanged. Thus, the suspensions made from stiff straight fibers are referred to as free suspensions. The magnitude of the x velocity component of the fibers v_s is quantified in Fig. 1(c) using particle image velocimetry (PIV) [29]. The specified flow rate is translated into an average velocity $v_a \equiv Q_0/A_b$ in the barrel, where A_b is the cross sectional area of the barrel. The average velocity in the nozzle is χv_a, which is controlled by a geometric parameter $\chi \equiv A_b/A_n$, where A_n is the cross sectional area of the nozzle. For the results in Fig. 1(c), $\chi \equiv A_b/A_n = 5$. The fibers in the nozzle moved at a velocity χ^* times faster than v_a. PIV results indicate $\chi^* \approx \chi$ throughout the extrusion process. In the barrel, the velocity of the straight fibers remained close to v_a.

To enhance entanglements among the fibers, we added mechanical oscillation to the JAWS fabrication method to make looped fibers with an average diameter $d = 60\ \mu$m, length $l = 4.5$ mm and aspect ratio $l/d = 75$ (Fig. 1(d) and Fig. A1). Each looped fiber has four permanent non-intersecting loops that have a typical dimension of 200 μm. Based on our experimental observations and imaging, the loops act like hooks to allow interlocking among the fibers (Fig. A2). Thus, the suspensions made from looped fibers are referred to as entangled suspensions. Similar to the free suspension, the same extrusion

experiment is carried out in (Fig. 1(e)) under the same flow rate and initial fiber volume fraction. For the suspension of looped fibers, the faster moving fibers in the nozzle were entangled with the fibers in the barrel. As a result, the fibers became more concentrated in the nozzle, as evident from the darker color in the images, and left excess water behind in the barrel. The magnitude of the x-velocity component of the fibers v_s is quantified in Fig. 1(f). The PIV results also indicate $\chi^* \approx \chi$ for looped fibers. The observed response is different from the stiff straight fibers, as the looped fibers in the barrel gradually accelerated from v_a to χv_a. We have also made entangled suspensions by using long and flexible fibers with aspect ratio = 360 [5]. Similar to the suspension made from looped fibers, the fiber volume fraction also increased in the nozzle leaving a more dilute suspension in the barrel (Fig. A3).

The approximation $\chi^* \approx \chi$ requires sufficiently high Q_0 and is one of the operating conditions when extruding a fiber suspension through a constriction (Fig. 1(g)). In particular, in the above setup when Q_0 is reduced to 1 ml/min, $\chi^* = 0$, the fibers remain clogged before the constriction and are unable to enter the nozzle. The clogging regime occurs due to a combination of fiber interactions with the wall, fiber stiffness, and the three-dimensional deformations at the constriction [30, 31], which are beyond the scope of this study. While such clogging or partial clogging are regularly observed for particles flowing through a constriction, the high flow rate regime where the suspension is concentrated is unique to the entangled fibers. For the rest of the paper, we will thus focus on this regime where the fibers move at the local average velocity in the nozzle, i.e., $\chi^* = \chi$.

Poroelastic model for the extrusion of an entangled suspension

As experimentally documented in the previous section, entangled suspensions respond to velocity variations at a constriction differently from free suspensions. To understand the mechanical response of an entangled fiber suspension under extensional deformations, we pulled a few fibers from a suspension of fibers while monitoring the pull-out force. The calculated stress-strain relationship is shown in Fig. A4. As fibers were pulled from the entangled suspension, a much higher stress was registered compared to similar measurements made for suspensions of straight fibers. For short stiff fibers, i.e., the free suspension, no stress can be measured, indicating the absence of entanglements. The results also showed that the looped fiber suspension overall had a linear response to stretching before the entanglements failed at a large strain of 600%.

Based on the above observations and measurements, we propose a uniaxial poroelastic extrusion model for a long barrel, as sketched in Fig. 2(a). Initially, a porous material is in a relaxed state in the barrel of an extrusion setup spanning distance L from the constriction on the right (Fig. 2(a)). The material has uniform porosity, defined as the volume fraction of the fluid $\phi_{f,0} = 1-\phi_{s,0}$. Starting from $t = 0$, a total flow rate Q_0 is then applied, creating a velocity v_a in the barrel. The entrance flow near the constriction is assumed to occupy a region $D \ll L$ (long barrel approximation). As the fibers enter the nozzle ($x = L$), they move at speed χv_a, resulting in the stretching of the entangled solids in the barrel. The flow is approximated as one dimensional in the domain between $0 \leq x \leq L$. The equations for uniaxial poroelastic deformation have been stated elsewhere [32, 33] and will be described briefly here.

In the Eulerian (laboratory) frame, the displacement field of the solid at time t is $u_s = x-X(x,t)$, where X is the reference position of the material. The

solid deformation changes the solid volume fraction. In the uniaxial geometry with uniform initial porosity, the deformation gradient $(1 - \frac{\partial u_s}{\partial x})^{-1}$ is equal to the volume fraction variation $\frac{1-\phi_{f,0}}{1-\phi_f}$, which leads to a relationship between u_s and the time-varying porosity field $\phi_f(x,t)$, i.e.,

$$\frac{\partial u_s}{\partial x} = \frac{\phi_f - \phi_{f,0}}{1 - \phi_{f,0}}. \tag{1}$$

A more rigorous derivation in tensor form can be found in [32]. The corresponding velocity of the solid is the material derivative of the displacement field: $v_s = \frac{Du_s}{Dt} = \frac{\partial u_s}{\partial t} + v_s \frac{\partial u_s}{\partial x}$, yielding $v_s = \frac{\partial u_s}{\partial t}/(1 - \frac{\partial u_s}{\partial t})$.

The total flux in the barrel v_a represents the total volume flow per area per time, which is an imposed constant value in our experiments, and is divided among the fluid velocity $v_f(x,t)$ and the solid based on their volume fractions:

$$v_a \equiv \phi_f v_f + (1 - \phi_f) v_s. \tag{2}$$

We assume the fluid flows relative to the solid according to Darcy's law [34]:

$$\phi_f(v_f - v_s) = -\frac{k(\phi_f)}{\mu}\frac{\partial p}{\partial x}, \tag{3}$$

where $k(\phi_f)$ is the porosity-dependent permeability, μ the viscosity of fluid, and p the pressure within the suspension. The continuity equation for the fluid is

$$\frac{\partial \phi_f}{\partial t} + \frac{\partial}{\partial x}(\phi_f v_f) = 0. \tag{4}$$

Combining Equations 2-4 we have a one-dimensional poroelastic equation:

$$\frac{\partial \phi_f}{\partial t} + \frac{\partial}{\partial x}\left(\phi_f v_a - (1 - \phi_f)\frac{k(\phi_f)}{\mu}\frac{\partial p}{\partial x}\right) = 0. \tag{5}$$

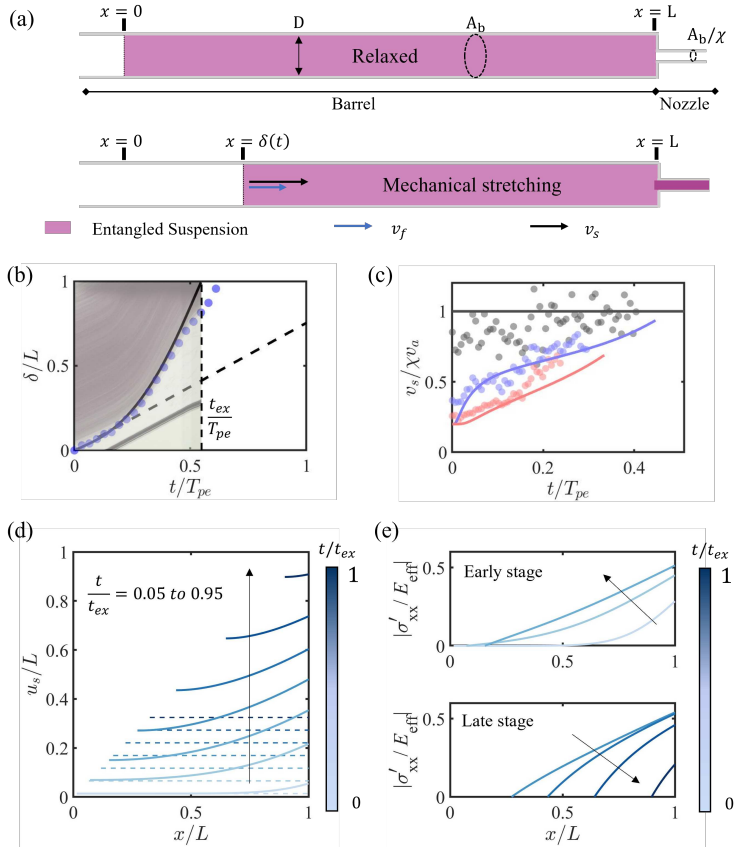

Fig. 2 Poroelastic model for the extrusion of entangled fibers. (a) A uniaxial model of a poroelastic material being extruded in a long straight tube. The solid phase is laterally confined and relaxed in the barrel (length L). The barrel cross section has typical diameter (or width for rectangular channels) D. The left, unconfined boundary of the solid phase is free of stress in the x direction. The ratio of the cross-sectional area between the barrel and nozzle is χ, where $\chi > 1$. When a constant flow rate Q_0 is applied from the barrel to the nozzle, a total flux of v_a is created in the barrel. The displacement of the left edge of the suspension is denoted by $x = \delta(t)$, with $\delta(0) = 0$. At $x = L$, the solid velocity v_s increases to χv_a, stretching the solid in the barrel. (b-e) Poroelastic model for the extrusion of looped fiber suspensions, as shown in Fig. 1(e,f). Actual experimental parameters and fitting parameter $F \equiv k_0 E_{\text{eff}} = 91$ nN are used in all panels, resulting in $\overline{v}_a = 0.63$. (b) The simulated (solid line) and experimentally measured (dots) left boundary displacement $\delta(t)$ of the suspension during extrusion. The dot size represents typical errors in the measurement. The inclined dashed line is the trajectory at constant velocity v_a. Kymograph of the center line of the setup is presented in the background. At t_{ex} all solid material has passed the constriction. T_{pe} is defined in Equation 9. The deviation of data from the fitted line, especially approaching t_{ex}, is due to the fibers coming in contact with the syringe at the end of the nozzle. (c) Comparison between the computed velocity profiles and measured PIV results at locations in Fig. 1(f) indicated by the corresponding colored triangles. Grey: nozzle ($x/L = 1$); blue: near constriction ($x/L = 0.75$); red: farther from constriction ($x/L = 0.4$). (d) The distribution of the normalized displacement field u_s/L during times up to approximately t_{ex} (solid lines) and the displacement field without elasticity (dashed lines) over the same time domain. Time interval between each line is $0.15t_{ex}$. Darker colors represents later times. (e) The normalized elastic stress $\sigma'_{xx}/E_{\text{eff}}$ at early stage (top panel) and late stage (bottom panel) of extrusion.

The total stress within the suspension is composed of the elastic stress of the entangled fiber network σ'_{xx} and hydrodynamic pressure p: $\sigma_{xx} = \sigma'_{xx} - p$. Neglecting inertia and in the absence of body forces, the effective stress σ'_{xx} (or "Terzaghi stress" [35]) among the elastic fiber network satisfies

$$\frac{\partial \sigma'_{xx}}{\partial x} = \frac{\partial p}{\partial x}. \tag{6}$$

Because the Young's modulus of the crosslinked PEGDA used in the experiments is much larger than the effective Young's modulus of the fiber network (100 kPa versus 100 - 1000 Pa), the deformations are assumed to originate solely from bending and rearrangements of the fibers. Based on the results from our pull-out tests, we use a linear elastic relation (Hooke's law) between the deformation and the entangled fiber stress, σ'_{xx}:

$$\sigma'_{xx} = E_{\text{eff}} \frac{\partial u_s}{\partial x}, \tag{7}$$

where E_{eff} is the effective Young's modulus of the suspension.

The permeability $k(\phi_f)$ is assumed to vary from its initial relaxed state k_0 like a randomly oriented suspension of fibers: [18]

$$\frac{k(\phi_f)}{k_0} = \frac{1-\phi_{f,0}}{\ln(1-\phi_{f,0}) + 0.931} \frac{\ln(1-\phi_f) + 0.931}{1-\phi_f}, \tag{8}$$

which is valid for $\phi_{f,0} > 0.7$. The absolute value of k_0 is not required in the model after nondimensionalization.

At the right boundary of the domain, $x = L$, we assume $v_s = \chi v_a$, which neglects the entrance flow region based on the long-barrel approximation. The above equations are to be solved for u_s, where $v_s = \chi v_a$ serves as a Neumann

boundary condition for the solid phase at $x = L$. The velocity at the left boundary $x = \delta(t)$ is to be calculated.

Nondimensionalization of equation 5 yields the poroelastic time scale for the dynamical response,

$$T_{pe} = \frac{\mu L^2}{E_{\text{eff}} k_0}. \tag{9}$$

The model is controlled by three independent dimensionless parameters, i.e., the strength of the imposed total flux that compares the flow time scale $T_f = L/v_a$ to the poroelastic time scale

$$\overline{v}_a = \frac{v_a \mu L}{E_{\text{eff}} k_0} = \frac{T_{pe}}{T_f}, \tag{10}$$

the cross sectional area ratio χ, and the initial porosity $\phi_{f,0}$. The equations are integrated using a Runge-Kutta scheme (adopted from [32]) in a moving boundary domain over the entire time the suspension spends in the barrel.

Comparison between model and experiments

To model the displacement and velocity variations during the extrusion of looped fibers, we compute the poroelastic model using the experimental values from Fig. 1 and a fitting parameter $F \equiv k_0 E_{\text{eff}}$. In Fig. 2(b) we compare the computed displacement of the left boundary $\delta(t)$ with the experimental results of the boundary of the fiber-rich region. The experimentally measured $\delta(t)$ initially moved at constant speed v_a, then accelerated for the rest of the extrusion. Using $F = 91$ nN, the simulated δ shows good agreement with the time variation of the experimental measurements. In comparison, paper pulp has a typical F of 30 nN at the same solid volume fraction [36]. All of the solid material has left the barrel by the time t_{ex}, which yields an average velocity $L/t_{ex} = 2.6 v_a$.

Using the same F, we next compare the velocity fields between the experiments and simulations. In Fig. 2(c), the measured velocities at the positions indicated by the colored triangles from Fig. 1(f) are compared with the simulation results at the same positions. The experimental velocity of the solid in the nozzle is close to χv_a despite variations in the PIV measurements due to limited lighting in the nozzle. Near the constriction (blue), the solid velocity starts from v_a at $t = 0$, then increases rapidly, followed by a more gentle increase, which is a feature observable in both the experiments and the simulations. The velocity increases at all positions in the barrel, but the rate of increase is higher near the constriction (blue versus red). Overall, the simulation captures the velocity evolution observed in the experiments both qualitatively and quantitatively.

Based on these validations of the model, Fig. 2(d) shows the displacement fields that are not readily observable in the experiments, which we compare with the displacement fields of a free suspension over the course of t_{ex}. In a free suspension, $E_{\text{eff}} = 0$ and the corresponding displacement field is uniform (flat) for all x. Without elastic stretching, the solids in the suspension across the domain will move at v_a. The difference between the two cases are obvious from the beginning of the extrusion. For the entangled suspension, the displacement field exceeds the free suspension at $x = L$, where the velocity difference between the solid and the fluid is the greatest. The difference in displacement then expands over time throughout the suspension.

In contrast to the flat displacement field in a free suspension, entanglements create a displacement gradient that translates into the strain and stress within the fiber network. Fig. 2(e) shows the internal elastic stress field during extrusion up to a time close to t_{ex}. At $x = L$, the stress starts to increase at $t = 0$, then peaks in the middle of the extrusion process. At other locations, the onset

of stress increase occurs at a later time. As a result of the linear relationship between the fluid volume fraction and the elastic stress from Equations 1 and 7, ϕ_f has similar dynamics to σ'_{xx} (Fig. A5).

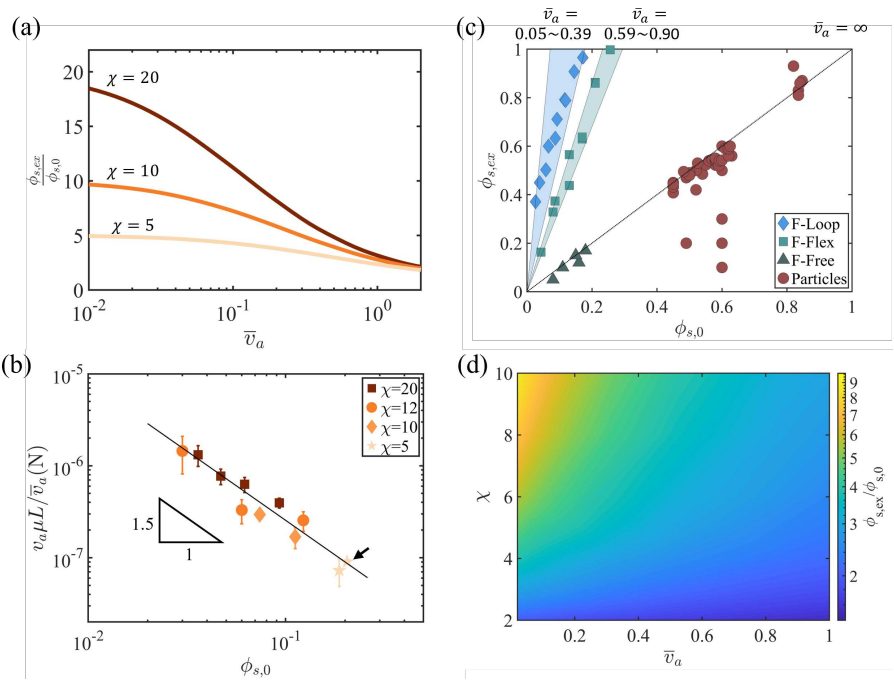

Fig. 3 $\phi_{s,ex}$ as a function of $\overline{v}_a$ and χ. (a) Computed $\phi_{s,ex}/\phi_{s,0}$ as a function of $\overline{v}_a$ at three different χs. Displayed curves use $\phi_{s,0} = 0.05$. The effect of $\phi_{s,0}$ on $\phi_{s,ex}/\phi_{s,0}$ is too small to be visible when $\overline{v}_a$ and χ are fixed A5. (b) Experimentally fitted $F_{exp} = k_0 E_{\text{eff}}$ as a function of $\phi_{s,0}$ at different χ. F_{exp} is calculated from fitted $\overline{v}_a$ using formula $F_{exp} = v_a \mu L/\overline{v}_a$. The error bars are calculated from five independent measurements. The experimental data of looped fibers from Fig. 1 is indicated by the black arrow. All experiments satisfy the condition $\phi_f > 0.7$ required in Equation 8. (c) $\phi_{s,ex}$ at different $\phi_{s,0}$ for different suspension materials. Circles are reported extrusion results from particle pastes made of ceramics [37–42] and polymers [7–10, 43]. The diamonds and triangles represent individual experiments performed with looped and straight fibers shown in Fig. 1, respectively. The squares represent results from long and flexible straight fibers. The experiments with fibers were performed in a syringe with χ equal to 20 and Q_0 equal to 8 ml/min. The blue and green regions represent model predictions at $\chi = 20$ at different ranges of $\overline{v}_a$; the dotted line represents $\phi_{s,ex} = \phi_{s,0}$ when $\chi = 1$ or $\overline{v}_a = \infty$. (d) The simulation result of $\phi_{s,ex}/\phi_{s,0}$ based on the poroelastic extrusion model as a function of χ and $\overline{v}_a$ at $\phi_{s,0} = 0.1$.

Extrudate volume fraction of entangled fiber suspensions

After being extruded through a constriction, the entangled fiber suspension changes its volume fraction significantly. We define $\phi_{s,ex}$ as the average extrudate volume fraction calculated based on the total extrusion time $\phi_{s,ex} \equiv \frac{L}{v_a t_{ex}}\phi_{s,0}$. Using the poroelastic extrusion model above, we can compute $\phi_{s,ex}$ as a function of $\overline{v}_a$ and χ. The results in Fig. 3(a) show how $\phi_{s,ex}/\phi_{s,0}$ varies with $\overline{v}_a$ for different values of χ. The third independent variable in the model $\phi_{s,0}$ has little effect on $\phi_{s,ex}$ (Fig. A5). Given the definitions, $1 \leq \phi_{s,ex}/\phi_{s,0} \leq \chi$, where the variations depend on $\overline{v}_a$: thus, the stronger the entangled network (smaller $\overline{v}_a$), the higher the $\phi_{s,ex}$.

We experimentally extruded looped fiber suspensions and measured $\phi_{s,ex}$ at different conditions of χ, $\phi_{s,0}$, Q_0 and L (Fig. A7 and Table A1). These measurements are fitted to the computational results by adjusting $\overline{v}_a$. Using measurable dimensional quantities v_a, L and μ, the fitted $\overline{v}_a$ thus allows the calculation of $F_{exp} \equiv v_a \mu L/\overline{v}_a$ based on experimental results. While k_0 and E_{eff} are a function of $\phi_{s,0}$, their specific relations are determined by the microstructure and entanglements of the suspension that are unknown at this point [44]. Given the same fiber geometry, however, their product F would have a universal relationship with $\phi_{s,0}$, independent of the extrusion conditions.

The calculated F_{exp} is shown in Fig. 3(b) as a function of $\phi_{s,0}$. The data show the relationship between F_{exp} and $\phi_{s,0}$ are conserved when different χ, L, v_a and A_b are used. The fitted power law has an exponent of -1.5 and R^2 value of 0.95. Rheological measurements of the shear modulus G' and yield stress of the looped fiber suspension show a power law relationship with $\phi_{s,0}$ with exponent of 3.0 and 3.6, respectively (Fig. A6). If E_{eff} follows the same power law as G' or the yield stress, k_0 would scale as $\phi_{s,0}$ to the power of -4.5 or -5.1, similar that of pulp suspensions and distinct from a suspension of

random rods [45] in the same range of $\phi_{s,0}$. This result demonstrates F_{exp} is a reasonable characterization of F using extrusion experiments.

Many other factors could contribute to the variations of F_{exp} reported in Fig. 3(b). In our continuum treatment of the fiber suspension, F takes into account the unique microstructure including the pore size for k_0 and entanglements for E_{eff}. When the micro-pores and entanglements of the suspension are properly averaged and pre-conditioned, F becomes primarily controlled by $\phi_{s,0}$ [46]. However, the experimentally derived F_{exp} relies on experimental conditions matching with the model, which are not perfect for several reasons. First, the finite length of the barrel means the entrance flow near the constriction will compromise the uniaxial assumption. Second, the real velocity of the fibers in the nozzle can be smaller than χv_a, especially when $\chi\phi_{s,0} \sim 1$ where volume exclusion occurs. Third, we assume the entangled fiber suspension deforms linearly (Equation 7) throughout the extrusion process, which may not be valid at large deformations. Despite these challenges, F_{exp} provides essential information on the suspension properties for the prediction of extrusion time and extrudate concentration.

Control of extrudate volume fraction in entangled and free suspensions

In the extrusion of particulate suspensions, the relative motion of solid and liquid typically reduces the volume fraction of the solid content in the extrudates [7–10, 37–43]. The driving forces are the hydrodynamic and frictional interactions among the particles and the wall [47]. In Fig. 3(c), we show representative results from the literature on the extrudate volume fractions of particulate pastes, where all the experiments were performed with spherical or near-spherical particles made of ceramics [37–42] and polymers [7–10, 43].

Except when there is leakage in the channel [41], all the results from the extrusion experiments produced extrudates with equal or lower solid content. Similar observations were also made in our experiments with free straight fibers with aspect ratio 72, which corresponds to free suspensions where $E_{\text{eff}} \to 0$ and thus $\overline{v}_a \to \infty$.

Extrudates with significantly higher volume fraction than the initial volume fractions are possible for entangled suspensions, such as the looped or long flexible fibers shown in Fig. A3. Using a syringe with $\chi = 20$, the ratio $\phi_{s,ex}/\phi_{s,0}$ of looped fibers ranges from 6.8 to 14, corresponding to $\overline{v}_a$ between 0.05 to 0.39. For long flexible fibers using the same syringe, $\phi_{s,ex}/\phi_{s,0}$ can range from 3.3 to 4.3 corresponding to $\overline{v}_a$ between 0.59 and 0.9. (Fig. 3(c)). At the same $\phi_{s,0}$, the extrudates from the looped fibers show higher volume fractions than from the long flexible fibers indicating higher F for the looped fibers, which could be explained by a higher Young's modulus of their entangled network. This observation is in agreement with the stiffer stress-strain relationship for the looped fiber suspension in the pull-out test (Fig. A4).

The ratio $\phi_{s,ex}/\phi_{s,0}$ of an entangled suspension can thus be controlled by varying the channel geometry χ and fluid-solid interactions through the parameter $\overline{v}_a$ (Fig. 3(d)). $\overline{v}_a$ can be adjusted by either varying the flow time scale, i.e., L/v_a, or the poroelastic response of the suspension through T_{pe} (in particular liquid viscosity, fiber shape, and flexibility). In the limit of small $\overline{v}_a$, $\phi_{s,ex}/\phi_{s,0} \approx \chi$ indicating stiff entanglement network or weak hydrodynamic interactions. In the limit of large $\overline{v}_a$, $\phi_{s,ex}/\phi_{s,0} \approx 1$, indicating soft entanglement network and strong hydrodynamic interactions. Large $\overline{v}_a$ often results in large deformation of the network that could lead to break down of the linear stress response (Equation 7) or total break up of the network as seen in the final stage of the pull-out test in Fig A4.

Compared to other entangled materials, such as nanofibrillated cellulose [7], microtubules [28] and sticky particles [27], the entangled microfibers are distinct in their combined properties of high permeability and strong entanglements, i.e. low $\overline{v}_a$. Such properties preserve the entangled network as a whole as the suspension passes a constriction. The mechanism and method for controlling the volume fraction variations of entangled suspensions in this work thus pave the way for future explorations of using these materials in healthcare, three-dimensional printing, or material repair.

Methods

Jet assisted wet spinning (JAWS) fiber synthesis

Poly(ethylene glycol) diacrylate (PEGDA) fibers were prepared in a jet assisted wet spinning (Fig. A1) setup. The assembly of the needles in JAWS was made with a 27 gauge (27G) needle bent to be within 2 mm distance to the end of a 34 gauge (34G) needle (Cellink, MA). The ends of both needles were immersed and placed near one side of a water-filled tank (9 cm by 9 cm in width and 12 cm in height). For making straight fibers, the position of the needle assembly was fixed. For making looped fibers, the needle assembly was mounted on a mechanical vibration generator (PASCO Scientific, CA). The vibration generator oscillates horizontally at 60 Hz frequency. The oligomer solution was composed of 80 vol % PEG-diacrylate (PEGDA, molecular weight = 575 g/mol), 16 vol % deionized (DI) water and 4 vol % 2-hydroxy-2-methylpropiophenone (photoinitiator). Less than 1 vol % reactive dye, acryloxyethyl thiocarbomoyl rhodamine B (Polysciences), was added to aid in visualizing the fibers. Water was supplied through the 34G needle at a constant flow rate of 0.5 ml/min and the oligomer solution was supplied through the 27G needle at a constant flow

rate of 5 μl/min, using syringe pumps (Harvard Apparatus). Unless otherwise stated, all chemicals were purchased from Sigma-Aldrich.

UV light was used to initiate the cross-linking reaction in the monomer jet. The UV light was supplied by a 365 nm LED light source (M365LP1, Thorlabs) focused through an objective to a 1 mm by 1 mm region. To make straight fibers, 60 ms ON and 40 ms OFF times or 550 ms ON and 50 ms OFF times of the UV light were used for fibers of aspect ratio (AS) 72 and 360, respectively. To make looped fibers 60 ms ON and 40 ms OFF times were used.

Extrusion visualization setup

The polydimethylsiloxane (PDMS) (Dow Sylgard 184) channels in Fig. 1 were plasma bonded to glass slides using a Corona Surface Treater (Electro-Technic Products, Inc.). The PDMS was formed on an acrylic mold milled by a CNC machine (Bantam tool). The channel has a uniform depth of 8 mm, a width of 10 mm in the barrel section and a width of 2 mm in the nozzle section, thus the ratio between the cross sectional areas of the barrel (A_b) and the nozzle (A_n) yield $\chi \equiv A_b/A_n = 5$. The barrel section has a total length of 45 mm and opens to atmosphere. The nozzle section has a total length of 40 mm. Before the experiments, the channel was placed vertically on a 5 ml HSW syringe mounted on a syringe pump (Harvard Apparatus). The fiber suspension was then poured into the channel and allowed to relax for 1 minute before a withdrawal flow rate of 8 ml/min was applied. Within the time of the experiment, the gravitational settling of the suspension is negligible. The video was taken with a DLSR camera (lens: Nikon Micro-Nikkor 85mm F/3.5) and recorded on a computer.

Extrusion experiments for E_{eff}

For the experimental results presented in Fig. 3(a) for the fiber suspensions, we used standard 5 ml and 3 ml syringes and modified 5 ml and 3 ml syringes (Norm-Ject, Luer Lock). Specific parameters can be found in Table A1. In modified syringes, the Luer section was cut and the opening was enlarged to a diameter of 4.2 mm. Before an extrusion experiment, the plunger was removed to pour the fiber suspension into the syringe. Next, the plunger was put back and adjusted to the desired volume. To accommodate the long barrel approximation in the poroelastic model, we ensured that the suspension occupied a length $L > 3.5D$.

Characterization of the physical properties of fibers and fiber suspensions

The width and length of fibers are measured using dilute fiber suspensions and microscope images using ImageJ software (ImageJ version 1.53e; NIH). The length and diameter of the fibers are taken as the average of approximately 50 fibers. The straight fibers with aspect ratio (AS) of 72 have length $l = 4.3 \pm 0.7$ mm and diameter $d = 59.6 \pm 2.0$ mm; the straight fibers with AS of 360 have length $l = 22 \pm 1.2$ mm and diameter $d = 60.4 \pm 1.7$ mm. The looped fibers have $l = 4.5 \pm 0.8$ mm and the loops on the looped fibers have a typical dimension of 204 ± 42 μm. The Young's modulus, E_y, of the polymerized PEG was measured with a tensile test below a balance (Mettler Toledo, OH), where a straight fiber was immersed in water and pulled at a constant rate of 40 μm/s. The measured E_y was in the range of 100 kPa to 300 kPa for five fibers that were measured.

The pull-out experiments from fiber suspensions were conducted with a 1 mm diameter glass rod made from an end-melted glass capillary (WPI, FL)

(Fig. A1). The rod was attached to the measurement hook below a balance (Mettler Toledo, OH) connected to a computer. The end of the rod had a drop of liquid epoxy and was immersed in a water bath (10 cm by 10 cm by 30 cm). A 5 ml syringe (VWR) was prepared with the Luer slip cut off and filled with 3 ml of fiber suspension. The syringe was moved up from directly underneath the rod until the epoxy touches the suspension. The epoxy was then cured with UV light to attach the fibers to the rod. The rod did not touch the syringe throughout the process. The pull-out experiment was carried out by moving the syringe down using a linear translation stage (NRT100, Thorlabs) at a constant velocity of 40 μm/s.

Rheological measurement of looped fibers suspensions

Rheological measurements were conducted on an Anton Paar MCR 301 rheometer with a 50 mm diameter sand-blasted parallel plate. The gap between the parallel plates was 1.0 mm. G' at a shear strain of 1% was obtained from oscillatory shear measurements using a frequency of 1.6 Hz.

Appendix A Extended Data

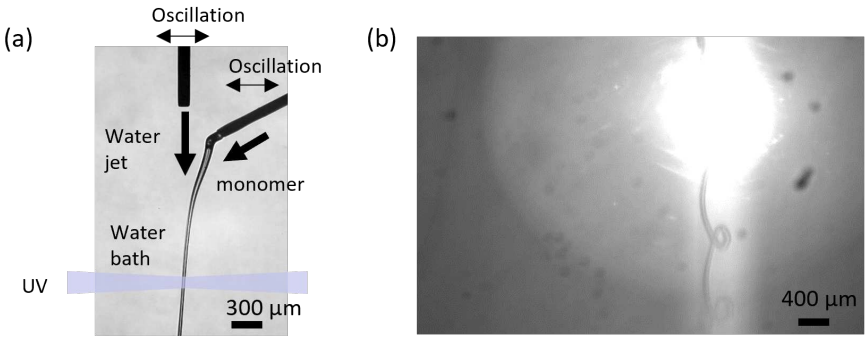

Fig. A1 Jet assisted wet spinning (JAWS). (a) Snapshot for JAWS. A monomer jet in a water bath is accelerated and thinned by a water jet. UV light is introduced downstream to crosslink the monomer. When making looped fibers, horizontal oscillation is added to both water jet and monomer jet. (b) Snapshot showing looped fibers being produced. The bright spot is the UV light spot.

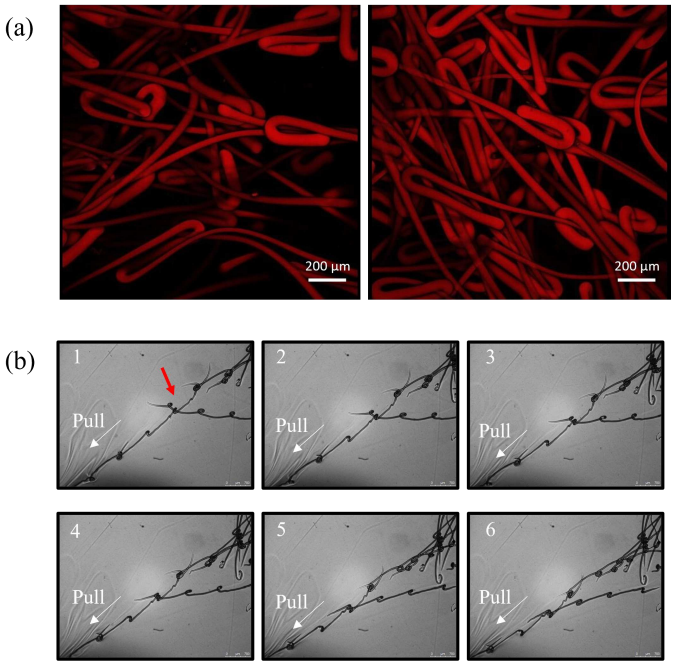

Fig. A2 (a) Confocal images of a suspension of looped fibers. (b) Time series (1-6) of an entanglement forming. A fiber is pulled to the left bottom corner while hooking with another fiber through the loop structure interaction, as indicated by the red arrow.

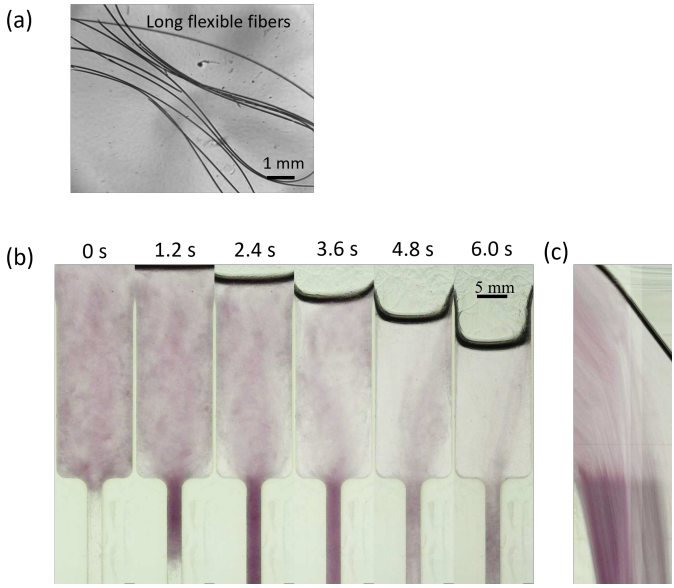

Fig. A3 (a) Shape of long flexible fibers. (b) Snapshots of suspensions of long flexible straight fibers flowing through a constriction when a constant flow rate of 8 ml/min is applied. The initial fiber volume fraction $\phi_{s,0}$ is 0.15. (c) Kymograph of the center line of the setup is presented, where the thick black line shows the water meniscus moving at v_a.

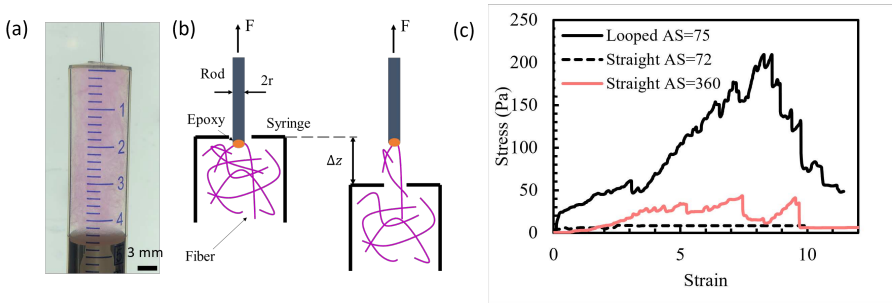

Fig. A4 (a) Snapshot of pull-out test of the looped fiber suspension (see *Materials and Methods* section for details). (b) Schematic of the pull out test. (c) Stress strain relationship of the pull out test of suspensions of looped and straight fibers. 'AS' stands for aspect ratio. All curves are measured at solid volume fraction ϕ_s of 0.15. The looped ($AS = 75$) and straight ($AS = 72$) fibers are used in Fig. 1 in the main text.

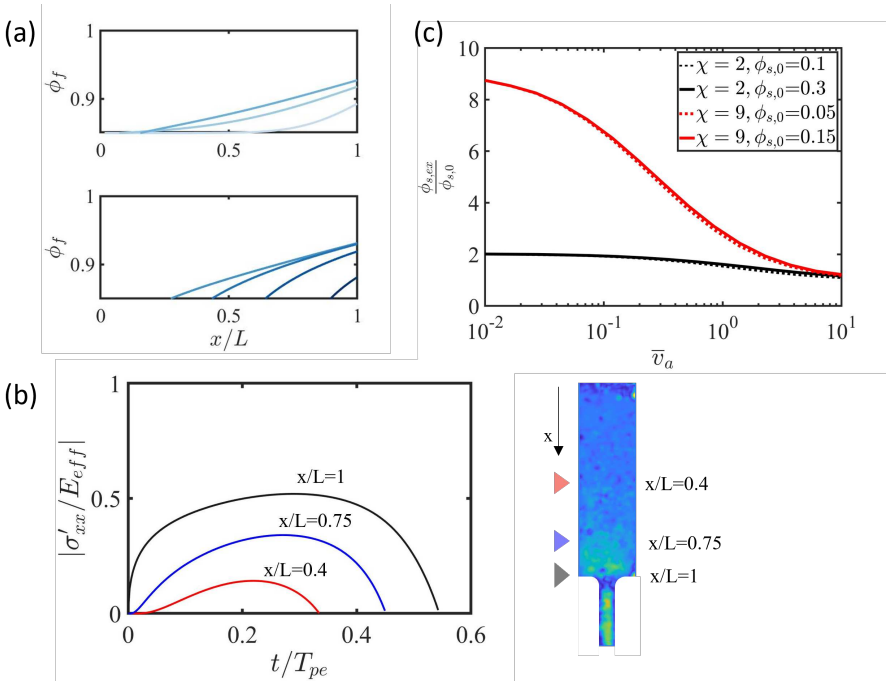

Fig. A5 (a) The volume fraction variation at the same time stamps as in Fig. 3(d) in the main text. The time increases from lighter blue to darker blue. (b) The σ'_{xx} at locations in the extrusion channel labeled by corresponding colored triangles.(c) The simulated $\phi_{s,ex}/\phi_{s,0}$ at different value of $\phi_{s,0}$ and $\overline{v}_a$ at $\chi = 2$ and $\chi = 9$.

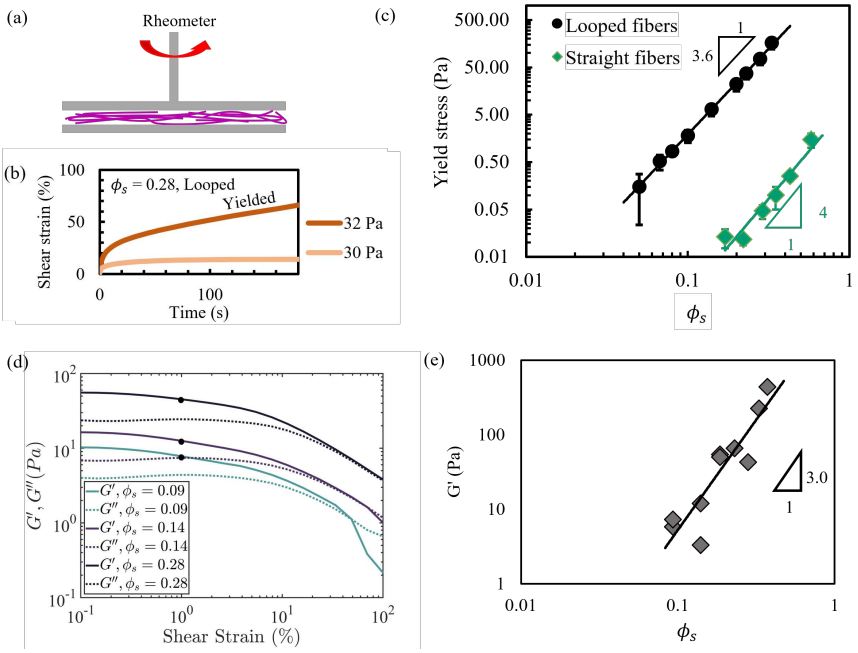

Fig. A6 (a) Rheology tests are performed with a sandblasted 50 mm parallel plate. The gap between the plates is 1 mm for all tests. (b) Strain response under constant shear stress of a looped fiber suspension at solid volume fraction of 0.28. When the applied stress is higher than the yield stress the shear strain will increase indefinitely (longer than 5 minutes in the test). (c) Yield stress of the entangled suspension made from looped fibers ($AS = 75$) and free suspension made from straight fibers ($AS = 72$) as a function of the solid volume fraction. (d) Storage (G') and Loss (G") moduli of looped fiber suspension at different solid volume fractions ϕ_s. The oscillatory frequency is 10 rad/s for all amplitude sweeps. (e) G' at 1% shear strain (dots in (d)) as a function of ϕ_s.

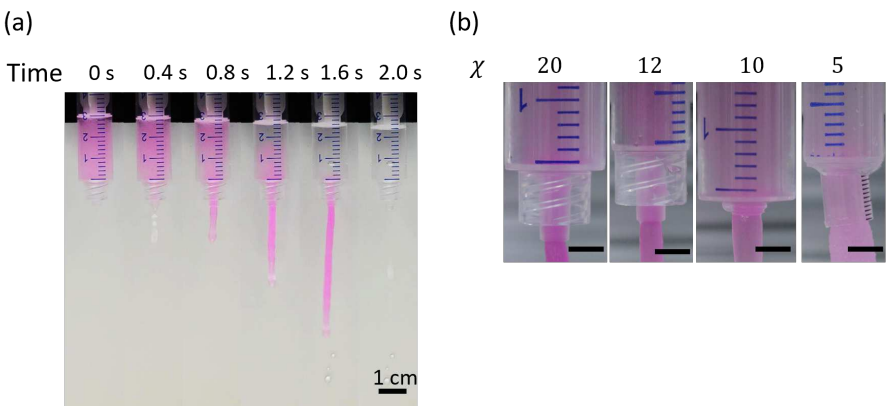

Fig. A7 (a) Typical time sequence when entangled fibers (looped) are extruded through a syringe. The magenta fibers started as distributed throughout the syringe. During extrusion the fibers expelled water from the suspension while being concentrated. (b) Snapshots during the extrusion of looped fibers using different extrusion geometries for data in Fig. 3(b) in the main text. The scale bar is 500 μm.

Table A1 Experimental conditions and $\phi_{s,ex}$ for data in Fig. 3 in the main text.

χ	A_b (mm^2)	L (mm)	Q_0 (ml/min)	$\phi_{s,0}$	$\phi_{s,ex}/\phi_{s,0}$
20	122.7	48.9	8	0.062	11.8±0.8
20	122.7	48.9	8	0.093	10.0±0.5
20	122.7	40.7	8	0.036	12.8±0.7
20	122.7	48.9	8	0.047	12.7±0.8
12	72.4	41.4	5	0.12	6.5±0.5
12	72.4	41.4	5	0.06	7.0±0.7
12	72.4	41.4	5	0.03	10.0±0.8
10	122.7	40.7	8	0.074	6.3±0.2
10	122.7	40.7	8	0.11	5.3±0.4
5	72.4	41.4	5	0.19	2.5±0.2

JAWS

We used jet assisted wet spinning (JAWS) to fabricate straight and looped poly(ethylene glycol) (PEG) microfibers from light-activated gelation chemistry. In JAWS, a slower monomer jet in a water bath is accelerated and thinned by a faster water jet (Fig. A1(a)). The ultraviolet (UV) light is introduced 2 cm downstream of the water jet needle to crosslink the monomer. When making looped fibers, horizontal oscillation is added to both the water jet and the monomer jet. Under the oscillation, the monomer jet not only acquires horizontal displacement but also adopts a different speed from the water jet [48]. As the monomer jet moves downstream, the speed difference develops into a vertical displacement difference. Together with the horizontal displacement from the oscillation, a looped structure is formed, which is retained permanently in the fibers by UV polymerization.

Extrusion of long straight flexible fibers

The long flexible fibers are made with JAWS with light on time 550 ms. Each fiber has length $l = 22$ mm, diameter $d = 60$ μm with aspect ratio (AS) of 360 (Fig. A3(a)). During the extrusion of a suspension of these fibers, the fibers in the nozzle were entangled with the fibers in the barrel, creating a higher velocity for the fibers in the barrel. As a result, the extrudate has a concentrated fiber suspension while excess water stayed in the barrel (Fig. A3(b)).

Pull-out test

The setup and schematic of the pull-out test is shown in Fig. A4(a) and (b). The stress is defined as the pull-out force divided by the cross sectional area of the probe, i.e., $F/\pi r^2$. The strain is defined as the probe displacement divided

by the probe diameter $2r$. The number of fibers being pulled out is between 5 and 12, but the stress and strain relationships are similar among different tests for the same suspension. Three typical stress-strain relationships are shown in Fig. A4(c). At the same solid volume fraction ϕ_s and similar fiber aspect ratio, the looped fibers show much higher entanglements as reflected in the high slope of the stress-strain curve. For straight fibers with AS of 360, significant entanglements also occur but are lower than the looped fibers.

Simulation results on ϕ_s, σ'_{xx}, and $\phi_{s,0}$

During poroelastic extrusion, the entangled fiber network stretches and dilutes the local solid volume fraction. Fig. A5(a) shows the solid volume fraction variations during the extrusion of looped fibers under the same condition as Fig. 1 in the main text. The dilution in the solid volume fraction ϕ_s (increase in ϕ_f) begins from $x = L$ and expands to $x = \delta$. A maximum is reached in in the middle of the extrusion process. In the Eulerian frame, the maximum in internal elastic stress is readily observable in Fig. A5(b). The highest level of stretching elastic stress among the fiber network occurs at the constriction. The stress disappears at free end of the suspension at $x = \delta$.

The extrudate volume fraction, presented as the the ratio $\phi_{s,ex}/\phi_{s,0}$, is predominantly determined by χ and $\overline{v}_a$. To fully describe the poroelastic model, $\phi_{s,0}$ also needs to be specified. We show the effect of $\phi_{s,0}$ in Fig. A5(c). The effect of $\phi_{s,0}$ on $\phi_{s,ex}/\phi_{s,0}$ is smaller than 4% for the two cases $\chi = 2$ and $\chi = 9$ across three decades of $\overline{v}_a$.

Rheology of fiber suspensions

The yield stress and shear modulus of the fiber suspensions are characterized in a rheometer (Fig. A6(a)). By applying a constant shear stress on a suspension

the suspension either deforms continuously over time (more than 5 minutes) or stops deforming after a finite time as shown in Fig. A6(b). We refer to the previous case as the yielded case and the latter case as the not yielded case. We adjust the applied stress to narrow the stress between the two cases until the difference is smaller than 30%. The yield stress is calculated between the two nearest yielded and not yielded cases (Fig. A6(c)).

The storage modulus of the suspension of looped fibers is measured on a rheometer using amplitude sweep as shown in Fig. A6(d). The storage modulus is higher than the loss modulus when the strain amplitude is smaller than 40 % to 100 %. As a function of the volume fraction, the storage modulus shows a power law relationship with an exponent of 2.95 in Fig. A6(e).

References

[1] Lim, J., Choi, G., Joo, K. I., Cha, H. J. & Kim, J. Embolization of vascular malformations via in situ photocrosslinking of mechanically reinforced alginate microfibers using an optical-fiber-integrated microfluidic device. *Advanced Materials* **33** (14), 2006759 (2021) .

[2] Macaya, D. & Spector, M. Injectable hydrogel materials for spinal cord regeneration: a review. *Biomedical materials* **7** (1), 012001 (2012) .

[3] Gao, Y., Li, Z., Huang, J., Zhao, M. & Wu, J. In situ formation of injectable hydrogels for chronic wound healing. *Journal of Materials Chemistry B* **8** (38), 8768–8780 (2020) .

[4] Qiu, W. *et al.* Nanofibers reinforced injectable hydrogel with self-healing, antibacterial, and hemostatic properties for chronic wound healing. *Journal of Colloid and Interface Science* **596**, 312–323 (2021) .

[5] Perazzo, A., Nunes, J. K., Guido, S. & Stone, H. A. Flow-induced gelation of microfiber suspensions. *Proceedings of the National Academy of Sciences* **114** (41), E8557–E8564 (2017) .

[6] He, J., Lee, S. S., Colakyan, M. & Kalyon, D. M. Viscoelastic properties and flow instabilities of aqueous suspensions of cellulosic fibers: Effects of a gelation agent on dispersion, rheology, and flow stability. *Polymer Engineering & Science* **61** (4), 1150–1165 (2021) .

[7] Rough, S., Bridgwater, J. & Wilson, D. Effects of liquid phase migration on extrusion of microcrystalline cellulose pastes. *International journal of pharmaceutics* **204** (1-2), 117–126 (2000) .

[8] O'Neill, R. E., Royer, J. R. & Poon, W. C. Liquid migration in shear thickening suspensions flowing through constrictions. *Physical review letters* **123** (12), 128002 (2019) .

[9] Haw, M. Jamming, two-fluid behavior, and "self-filtration" in concentrated particulate suspensions. *Physical review letters* **92** (18), 185506 (2004) .

[10] Kulkarni, S. D., Metzger, B. & Morris, J. F. Particle-pressure-induced self-filtration in concentrated suspensions. *Physical Review E* **82** (1), 010402 (2010) .

[11] Barnes, H. Shear-thickening ("dilatancy") in suspensions of nonaggregating solid particles dispersed in newtonian liquids. *Journal of Rheology* **33** (2), 329–366 (1989) .

[12] Huber, P., Carré, B. & Petit-Conil, M. The influence of tmp fibre flexibility on flocculation and formation. *BioResources* **3** (4), 1218–1227 (2008) .

[13] Negi, V. & Picu, R. Tensile behavior of non-crosslinked networks of athermal fibers in the presence of entanglements and friction. *Soft Matter* **17** (45), 10186–10197 (2021) .

[14] Ban, E., Barocas, V. H., Shephard, M. S. & Picu, C. R. Effect of fiber crimp on the elasticity of random fiber networks with and without embedding matrices. *Journal of Applied Mechanics* **83** (4) (2016) .

[15] Jarvis, P., Jefferson, B., Gregory, J. & Parsons, S. A. A review of floc strength and breakage. *Water research* **39** (14), 3121–3137 (2005) .

[16] Buck, G. & Simon, J. The spectrum of filament entanglement complexity and an entanglement phase transition. *Proceedings of the Royal Society A: Mathematical, Physical and Engineering Sciences* **468** (2148), 4024–4040 (2012) .

[17] Wyart, M., Liang, H., Kabla, A. & Mahadevan, L. Elasticity of floppy and stiff random networks. *Physical review letters* **101** (21), 215501 (2008) .

[18] Jackson, G. W. & James, D. F. The permeability of fibrous porous media. *The Canadian Journal of Chemical Engineering* **64** (3), 364–374 (1986) .

[19] Picu, R. Mechanics of random fiber networks—a review. *Soft Matter* **7** (15), 6768–6785 (2011) .

[20] Vermeulen, M. F., Bose, A., Storm, C. & Ellenbroek, W. G. Geometry and the onset of rigidity in a disordered network. *Physical Review E* **96** (5), 053003 (2017) .

[21] Derakhshandeh, B., Kerekes, R., Hatzikiriakos, S. & Bennington, C. Rheology of pulp fibre suspensions: A critical review. *Chemical Engineering Science* **66** (15), 3460–3470 (2011) .

[22] Bennington, C., Kerekes, R. & Grace, J. The yield stress of fibre suspensions. *The Canadian Journal of Chemical Engineering* **68** (5), 748–757 (1990) .

[23] Hubbe, M. A. *et al.* Rheology of nanocellulose-rich aqueous suspensions: a review. *BioResources* **12** (4), 9556–9661 (2017) .

[24] Nunes, J. K. *et al.* Fabricating shaped microfibers with inertial microfluidics. *Advanced Materials* **26** (22), 3712–3717 (2014) .

[25] Kessel, B. *et al.* 3d bioprinting of macroporous materials based on entangled hydrogel microstrands. *Advanced Science* **7** (18), 2001419 (2020) .

[26] Pääkkö, M. *et al.* Enzymatic hydrolysis combined with mechanical shearing and high-pressure homogenization for nanoscale cellulose fibrils and strong gels. *Biomacromolecules* **8** (6), 1934–1941 (2007) .

[27] Muir, V. G. *et al.* Sticking together: Injectable granular hydrogels with increased functionality via dynamic covalent inter-particle crosslinking. *Small* 2201115 (2022) .

[28] Qu, Z. *et al.* Persistent fluid flows defined by active matter boundaries. *Communications Physics* **4** (1), 1–9 (2021) .

[29] Thielicke, W. & Stamhuis, E. Pivlab–towards user-friendly, affordable and accurate digital particle image velocimetry in matlab. *Journal of open research software* **2** (1) (2014) .

[30] Souzy, M., Zuriguel, I. & Marin, A. Transition from clogging to continuous flow in constricted particle suspensions. *Physical Review E* **101** (6), 060901 (2020) .

[31] Lindner, A. Flow of complex suspensions. *Physics of fluids* **26** (10), 351–10945 (2014) .

[32] MacMinn, C. W., Dufresne, E. R. & Wettlaufer, J. S. Large deformations of a soft porous material. *Physical Review Applied* **5** (4), 044020 (2016) .

[33] Ockendon, H. & Terrill, E. A mathematical model for the wet-spinning process. *European Journal of Applied Mathematics* **4** (4), 341–360 (1993) .

[34] Darcy, H. *Les fontaines publiques de la ville de Dijon: exposition et application...* (Victor Dalmont, 1856).

[35] Terzaghi, K., Peck, R. B. & Mesri, G. *Soil mechanics in engineering practice* (John Wiley & Sons, 1996).

[36] Paterson, D. T., Eaves, T. S., Hewitt, D. R., Balmforth, N. J. & Martinez, D. M. One-dimensional compression of a saturated elastoviscoplastic medium. *Physical Review Fluids* **7** (5), 054303 (2022) .

[37] Rabideau, B. D. *et al.* Internal flow characteristics of a plastic kaolin suspension during extrusion. *Journal of the American Ceramic Society* **95** (2), 494–501 (2012) .

[38] Liu, H. & Leu, M. C. Liquid phase migration in extrusion of aqueous alumina paste for freeze-form extrusion fabrication. *International Journal of Modern Physics B* **23** (06n07), 1861–1866 (2009) .

[39] Liu, H., Liu, J., Leu, M. C., Landers, R. & Huang, T. Factors influencing paste extrusion pressure and liquid content of extrudate in freeze-form extrusion fabrication. *The International Journal of Advanced Manufacturing Technology* **67** (1), 899–906 (2013) .

[40] Habib, M., Baroud, G., Gitzhofer, F. & Bohner, M. Mechanisms underlying the limited injectability of hydraulic calcium phosphate paste. *Acta Biomaterialia* **4** (5), 1465–1471 (2008) .

[41] Yu, A., Bridgwater, J., Burbidge, A. & Saracevic, Z. Liquid maldistribution in particulate paste extrusion. *Powder Technology* **103** (2), 103–109 (1999) .

[42] Khelifi, H., Perrot, A., Lecompte, T., Rangeard, D. & Ausias, G. Prediction of extrusion load and liquid phase filtration during ram extrusion of high solid volume fraction pastes. *Powder Technology* **249**, 258–268 (2013) .

[43] Altobelli, S., Fukushima, E. & Mondy, L. Nuclear magnetic resonance imaging of particle migration in suspensions undergoing extrusion. *Journal of Rheology* **41** (5), 1105–1115 (1997) .

[44] Sevostianov, I. & Kachanov, M. Connections between elastic and conductive properties of heterogeneous materials. *Advances in applied mechanics* **42**, 69–252 (2009) .

[45] Paterson, D. T., Eaves, T. S., Hewitt, D. R., Balmforth, N. J. & Martinez, D. M. On two-phase modeling of dewatering pulp suspensions. *AIChE Journal* **67** (9), e17277 (2021) .

[46] Costa, A. Permeability-porosity relationship: A reexamination of the kozeny-carman equation based on a fractal pore-space geometry assumption. *Geophysical research letters* **33** (2) (2006) .

[47] O'Neill, R. *et al.* Extent and mechanism of phase separation during the extrusion of calcium phosphate pastes. *Journal of Materials Science: Materials in Medicine* **27** (2), 1–13 (2016) .

[48] Pope, S. B. *Turbulent flows* (Cambridge university press, 2000).